CONF-960202--17

LA-UR- 96- 668

Title: In situ observation of defect growth beyond the irradiated region in yttria-stabilized zirconia induced by 400 keV xenon ion-beam at -90 and 30 ^{o}C

RECEIVED
APR 12 1996
OSTI

Author(s): Ning Yu, Kurt E. Sickafus, Padma Kodali, and Michael Nastasi

Submitted to: J. Nuclear Materials (1996)

Los Alamos
NATIONAL LABORATORY

MASTER

Los Alamos National Laboratory, an affirmative action/equal opportunity employer, is operated by the University of California for the U.S. Department of Energy under contract W-7405-ENG-36. By acceptance of this article, the publisher recognizes that the U.S. Government retains a nonexclusive, royalty-free license to publish or reproduce the published form of this contribution, or to allow others to do so, for U.S. Government purposes. The Los Alamos National Laboratory requests that the publisher identify this article as work performed under the auspices of the U.S. Department of Energy.

Form No. 836 R5
ST 2629 10/91

DISTRIBUTION OF THIS DOCUMENT IS UNLIMITED

In situ observation of defect growth beyond the irradiated region
in yttria-stabilized zirconia
induced by 400 keV xenon ion-beam at -90 and 30 °C

Ning Yu *, Kurt E. Sickafus, Padma Kodali, and Michael Nastasi
Materials Science and Technology Division
Los Alamos National Laboratory, Los Alamos, New Mexico 87545, USA

ABSTRACT

Single crystals of yttria-stabilized zirconia (YSZ) were irradiated with 400 keV Xe ion-beam at room temperature and -90 °C. Defect growth was monitored *in situ* with Rutherford Backscattering and ion channeling (RBS/C) techniques using a 2 MeV He ion-beam. The irradiated YSZ was observed to consist of a 60 nm defect-denuded top layer, followed by a highly disordered layer. Ion channeling revealed that the degree of lattice disorder saturated at 70% of the random level in the bottom layer. At a dose of $3x10^{16}$ Xe/cm^2, this layer extended to a depth of 160 nm, well beyond the irradiated depth (<110 nm). Cross-sectional transmission electron microscopy observations along with RBS measurements are interpreted as indicating the presence of small Xe precipitates with an average diameter of 3 nm, uniformly distributed over the 20-110 nm depth. The study demonstrated that point defects generated in the Xe-irradiated region diffused and grew into more stable structural defects in the greater depth beyond the irradiated region.

Presented at the TMS'96 Meeting and submitted to J. Nuclear Materials, 1996.
* Corresponding author, permanent address: Semiconductor Process and Device Center, Texas Instruments, Inc., MS 944, P.O. Box 655012, Dallas, Texas 75265, USA.

1. Introduction

Many studies have focused on searching for radiation resistant ceramics and on understanding their radiation responses [1,2]. Magnesium aluminate spinel ($MgAl_2O_4$) has been demonstrated to be one of the most radiation resistant oxides under fast neutron irradiation [3-6] and ion irradiation [7] at elevated temperature up to 10-250 displacements per atom (dpa). However, it has been observed that spinel undergoes phase transformations from its equilibrium phase through an intermediate crystalline phase to an amorphous phase under ion irradiation at cryogenic temperatures [8,9]. This indicates that point-defect mobility that varies with irradiation temperature plays an important role during microstructural evolution in spinel. Therefore, we have extended our study on temperature dependence of radiation effects to other relevant oxides, including alpha-alumina (α-Al_2O_3) [10], geikielite ($MgTiO_3$) [10], ilmenite ($FeTiO_3$) [10], magnesia (MgO), rutile (TiO_2), and yttria-stabilized zirconia (YSZ). All these studies have taken great advantage of the *in situ* ion beam facility at Los Alamos National Laboratory (LANL) [11,12].

Previous studies [13,14] have shown that YSZ cannot be amorphized by Xe ion irradiation at room temperature. Transmission electron microscopy (TEM) studies revealed that high doses of Xe irradiation, $3\text{-}10 \times 10^{16}$ Xe/cm^2, into a TEM thin foil of YSZ resulted in formation of solid or fluid Xe embedded in the film. In this study, we have examined *in situ* the kinetics of radiation damage accumulation in YSZ induced by 400 keV Xe ion irradiation at temperatures of 30 and -90 °C. The radiation damage behavior was found to be the same at these two temperatures. The irradiated YSZ was observed to consist of a defect-denuded top layer of 60 nm thickness, followed by a highly disordered layer. The lattice disorder reached a saturation level in the bottom layer while its thickness increased towards a depth (160 nm) deeper than the irradiated depth (<110 nm). The study demonstrated that point defects generated in the Xe-irradiated region diffused and grew into larger size extended defects in the depth beyond the irradiated region.

2. Experiment

YSZ single crystals (ZrO_2), containing 9.4 mol.% Y_2O_3 and in a dimension of 10x10 mm^2 width and 0.5 mm thickness, were used in this study. The samples, oriented along the (001) axis and polished to an optical finish, were coated with a 20 nm carbon film to avoid surface charging for ion irradiation and ion-beam analysis. The ion irradiation experiments were performed at the

LANL *in situ* ion beam facility [11,12]. The LANL facility consists of a 200 kV ion implanter beamline and a 3 MV tandem ion beamline, respectively, for ion irradiation and ion-beam analysis, i.e., Rutherford backscattering and ion channeling (RBS/C) measurement, on a bulk single crystal sample, as shown in Fig. 1. An YSZ sample for the *in situ* experiment was mounted onto a sample stage with silver paint. The orientation and translational motions of the sample were controlled by a multi-axis goniometer. Prior to ion irradiation, the 2 MeV He^+ ion-beam from the tandem accelerator was aligned along the (011) axis of the unirradiated YSZ sample using RBS/C measurements. This orientation was kept throughout the entire *in situ* experiment to ensure the same channeling measurement conditions.

Radiation damage was introduced by 400 keV Xe^{2+} ion-beam incident at a 15° angle to the sample normal at temperatures of 30 and -90 °C. Radiation-induced lattice disorder was monitored through a sequential RBS/C measurement up to a charge of 4 μC following each incremental dose of Xe irradiation. The irradiation and analysis beam spots were co-centered on the sample surface with beam sizes of about 7 and 2 mm in diameter. The irradiation doses varied from $2x10^{13}$ to $3x10^{16}$ Xe/cm^2 with the irradiation beam flux maintained at ~$1x10^{13}$ Xe/cm^2-s. The irradiation experiment at room temperature was first performed and proceeded until the lattice disorder in the irradiated YSZ reached a certain saturation level. Then the sample was translated to set an unirradiated area and cooled to -90 °C for a second irradiation experiment. The projected range and the damage peak of 400 keV Xe ions at a 15° incident angle were estimated to be 75 and 50 nm, respectively, by the TRIM code [15] using a mass density of 5.6 g/cm^3 for YSZ. The damage level in the peak damage region was estimated to be 27 dpa for a dose of $1x10^{16}$ Xe/cm^2 assuming a displacement energy of 40 eV for all elements. The peak concentration of implanted Xe was about 2 at.% for $1x10^{16}$ Xe/cm^2 in YSZ.

Following the *in situ* experiments, the irradiated YSZ samples were further examined with RBS/C at room temperature. The samples were then prepared into electron transparent specimens for cross-sectional transmission electron microscopy (XTEM) examination. The radiation-induced microstructures were examined in a Philips CM 30 microscope operated at 300 kV using bright-field and dark-field XTEM techniques.

The LANL facility plays a complementary role to the high-voltage electron microscopy and tandem (HVEM-tandem) facility at Argonne National Laboratory (ANL). Fig. 1 shows comparison of the LANL *in situ* experiment with the ANL *in situ* experiment. The ANL facility

combines a 2 MV tandem ion beamline with an 1 MV electron microscope to perform ion irradiation and electron diffraction on an electron-transparent TEM thin foil, 50 nm thick and mounted on a TEM grid. The LANL experiment effectively determines the depth profile of radiation damage and the evolution of lattice disorder, while the ANL experiment directly monitors the radiation-induced phase transformations. In the ANL experiment, the TEM thin foil may limit the irradiation beam current in order to avoid the beam heating effect, and it may also have a surface effect where point defects annihilate at the surfaces to delay phase transformations. In the LANL experiment, the much larger area of a bulk sample allows a higher irradiation-beam current and causes less surface effect. For a large bulk sample, a set of irradiation experiments can be conducted in series at different temperatures by translating the sample without breaking the vacuum (Fig. 1).

The LANL *in situ* capability enhances the experimental efficiency typically by one order of magnitude and improves the experimental reliability as compared to conventional *ex situ* experiments. The conditions of the sample surface, the ion irradiation, the channeling alignment, and the characterization contribute to the uncertainty of the *ex situ* experiments. However, these variations are significantly minimized in the *in situ* experiments. Furthermore, during an *in situ* experiment, we can dynamically monitor the changes in the damage profile and control the incremental irradiation dose correspondingly. Therefore, radiation-induced phenomena can be carefully evaluated and resolved, and the corresponding microstructures can be determined by further *ex situ* TEM examination. The *in situ* experiment also maintains the same experimental environment for both irradiation and characterization of the sample. This eliminates the possibility of altering the sample conditions for the characterization purposes. Experimental results are thus more reliable for *in situ* measurements as compared to *ex situ* measurements.

3. Results

Fig. 2 shows some representatives of 18 sequential *in situ* (011) RBS/C spectra from the YSZ crystal following the 400 keV Xe irradiations at room temperature. Minimum backscattering yield, defined as the RBS yield ratio of an aligned spectrum to a random spectrum, is a measure of the degree of crystal quality or lattice disorder. A minimum yield of 10% for the Zr signal near the sample surface indicates good single crystallinity of the unirradiated sample. Following the irradiation of 1.5×10^{15} Xe/cm^2, a damaged layer appears around the damage peak in the depth of

60 nm, as indicated by the higher dechanneling yield in the channeling spectrum. However, the 60 nm top layer remains defect-denuded. After the irradiation to 5×10^{15} Xe/cm^2, no significant increase in the dechanneling is observed within the top layer. However, it is intriguing to note that the damaged layer grows deeper. The sharp interface between the bottom damaged zone and the top denuded zone is retained. At this stage, the damage-growing front in the 120 nm depth is definitely beyond the Xe-irradiated layer (<110 nm). As the irradiation dose increases to 1.5x - 3×10^{16} Xe/cm^2, a significant increase in the channeling yield in the top layer is observed. However, this increase is in part due to the overlap of the implanted Xe signal with the Zr signal. Excluding the contribution of the Xe signal, the minimum yield in the top layer is estimated to be less than 50%. The sharp interface between the surface denuded zone and the underlying damaged zone is maintained. The damaged zone is extended to a depth of 160 nm at a dose 3×10^{16} Xe/cm^2 with the minimum yield saturated at 70% of the random level. This indicates saturation of lattice disorder in the bottom zone.

Similar behavior of radiation damage is observed in YSZ irradiated with Xe ions at -90 °C, as shown by *in situ* RBS/C spectra taken at the same temperature in Fig. 3. Minimum yield appears to be 7% for the Zr in the unirradiated YSZ. The lower minimum yield value, as compared to that obtained at room temperature (10% in Fig. 2), is due to the reduction in lattice vibration at a lower temperature. A defect-denuded top layer is retained in the YSZ irradiated to doses of 1.5-5×10^{15} Xe/cm^2, followed by a heavily damaged layer starting in the 60 nm depth. Following sequential irradiations, the interface between the top and bottom layer remains unchanged while the bottom layer grows to a depth of 160 nm. The minimum yield of the bottom layer saturates at 70% of the random level to a dose of 3×10^{16} Xe/cm^2. A big hump that appears at the shoulder of the surface Zr in the random spectrum, taken from the 3×10^{16} Xe/cm^2 irradiated YSZ, is caused by the implanted Xe signal.

The kinetics of radiation damage accumulation in YSZ are determined from the sequence of *in situ* RBS/C spectra following the Xe irradiations. Fig. 4 shows the values of minimum yield from the heavily damaged zone for the Zr sublattice as a function of irradiation dose and temperature. The kinetic curve of room temperature shows a rapid rise in the minimum yield from 10% to 60% as the irradiation dose increases from 0 to 2.5×10^{15} Xe/cm^2. The degree of lattice disorder in this zone then levels off at a dose of 2.5×10^{15} Xe/cm^2 and the minimum yield only increases slightly from 60% to 70% as the dose increases to 3×10^{16} Xe/cm^2. This indicates that the lattice disorder

saturates for a dose of $2.5x10^{15}$ Xe/cm^2. The kinetic curve of -90 °C behaves similarly as that of 30 °C. Overall, there is a reduction of about 0.03 in the minimum yield for the -90 °C curve as compared to that of 30 °C. This can be solely attributed to the temperature dependence of the lattice vibration. In a defective crystal, both the lattice disorder and the lattice vibration add to the minimum yield. A decrease in the temperature results in a decrease in the lattice vibration that reduces the minimum yield. Taking the lattice vibration into account, the room temperature curve falls onto the low temperature curve. The results in Fig. 4 indicate that the damage accumulation induced by Xe irradiation is independent of the irradiation temperature, at least in the range from -90 to 30 °C.

The independence of damage accumulation on the irradiation temperature is further confirmed by *ex situ* RBS/C measurement. Fig. 5 shows (001) RBS/C spectra acquired at room temperature from the YSZ crystals irradiated to $3x10^{16}$ Xe/cm^2 at 30 and -90 °C, respectively. The profiles of lattice disorder for the Zr are identical following the Xe irradiations at two different temperatures. A small step near the edge of the surface Zr represents the implanted Xe. Simulation [16] of the random spectrum from the $3x10^{16}$ Xe/cm^2 irradiated YSZ reveals a relatively uniform distribution of 4 at.% Xe over the depth 20-110 nm. The heavily damaged zone is found to distribute in the depths of 60-160 nm. The TRIM code [15] predicts a near Gaussian distribution for the implanted Xe in YSZ. The uniform distribution of Xe determined by RBS indicates that the implanted Xe is significantly redistributed during the high dose of Xe irradiation. Furthermore, the heavily damaged zone is extended beyond the Xe-distributed zone. These observations indicate that the implanted Xe and the point defects are highly mobile in YSZ and their mobilities also appear to be independent of irradiation temperature from -90 to 30 °C.

The radiation-induced microstructures were examined on a YSZ sample irradiated to $3x10^{16}$ Xe/cm^2 at -90 °C using bright-field and dark-field XTEM techniques. Fig. 6(a) is a dark-field XTEM image taken with a $[\bar{1}\bar{1}1]$ diffraction vector. Three microstructural zones are distinct in the image along the Xe-irradiation direction (vertical on the page). The top zone, labeled "1", of 80 nm thickness shows a uniform distribution of small clusters with an average diameter of 3 nm. The second zone, labeled "2", of 100 nm thickness exhibits much larger extended defects with sizes of 5-20 nm. On the top portion of zone "2", about 40 nm thick, a mixture of small clusters and large structural defects are visible. The thickness of the zone "1" is close to that of the defect-denuded zone determined by RBS measurement (Figs. 3 and 5). Except for the small clusters, no large

structural defects are visible in this zone, in support of the RBS/C observation of the defect-denuded zone. The cluster features are similar to those observed in the $2x10^{17}$ Xe/cm^2 implanted MgO [17], which were identified as solid or fluid Xe precipitates. The cluster diameters in Fig. 6(a), however, appear to be much smaller than those in the MgO (10-50 nm) probably due to the big Xe dose difference in these two cases. These smaller clusters can be interpreted as precipitates of solid Xe because fluid Xe forms in much larger sizes (> 10 nm) [13]. The zone "2" containing larger extended defects represents the heavily disordered zone, as observed by the channeling measurement in Fig. 5. The nature of the extended defects is under further investigation. A transition layer between the zones "1" and "2" indicates that part of the Xe precipitated zone overlaps with the highly disordered zone. Inset microdiffraction patterns in Fig. 6(b), (c), and (d) were taken with short exposure times from the zones "1, 2, and 3", using a convergent electron-beam of 50 nm in diameter. No extra diffraction spots were observed from the zone "1". Due to the short exposure times and the small sampling area, the additional reflections from solid Xe may not be detectable [13]. These diffraction patterns are identical and indicate that no phase transformation occurs in the Xe-irradiated zone and the highly defected zone.

4. Discussion

By combining the RBS results with the XTEM results, schematic drawings are plotted in Fig. 7, showing the evolution of the distributions for implanted Xe ions and structural defects following the low dose to high dose of Xe irradiation. In the early stage of Xe irradiation, the implanted Xe has a near Gaussian distribution centered at a depth of 75 nm, while the damage profile peaks at a shallower depth, 50 nm. A high dose of Xe irradiation results in significant accumulation of Xe and production of radiation damage in the irradiated layer to a depth of 110 nm. The implanted Xe and the point defects produced by cascade collisions appear to be mobile. A highly disordered zone initially develops near the damage peak and then gradually grows deeper. The lattice disorder reaches a saturation level in the heavily damaged zone and more point defects diffuse through this layer to make it grow thicker. In contrast, the top layer of 60 nm thickness remains relatively defect-denuded up to high doses. Accompanying the growth of the disordered zone, the in- and out-diffusion of implanted Xe results in a uniform distribution of Xe precipitates over the depth of 20-110 nm.

The study clearly demonstrates the layer-by-layer growth of lattice disorder towards the deeper region beyond the irradiated region. It indicates that point defects generated in the irradiated region can diffuse through the highly disordered layer to grow new defects even at -90 °C. This presents the evidence that radiation-induced point defects are highly mobile in YSZ. Therefore, a high population of nonequilibrium point defects can readily annihilate within the irradiated region or transport out of the irradiated region and annihilate into sinks or form more stable defect structures. Only the inward flux of point defects is expected to contribute to the growth of defect structures beyond the irradiated region. Two obvious factors can cause the inward flux, (a) concentration gradient of the generated point defects and (b) strain field induced by implanted Xe and stabilized defects. Fracture toughness of Xe-irradiated samples, measured by indentation techniques, have revealed a 2-fold increase as compared to unirradiated samples. The higher fracture toughness confirms the presence of compressive stress in the Xe-irradiated layer. The compressive stress is consistent with a high concentration of Xe as well as some structural defects within the irradiated layer. The compressive stress may provide a significant driving force for inward diffusion of point defects.

Another important observation from Figs. 2-5 is that radiation damage accumulation in YSZ behaves the same at two different temperatures. Point-defect mobility appears not to change over the temperature from -90 to 30 °C. Furthermore, no amorphization is observed in the YSZ irradiated with 400 keV Xe ions up to $3x10^{16}$ Xe/cm^2 at -90 °C with a peak damage level equivalent to 110 dpa. The maximum lattice disorder saturates at the same level following irradiation at two different temperatures, as indicated by the 70% minimum yield. The defect saturation is consistent with that for 240 keV Xe irradiation at room temperature [13]. A recent study has also shown that no amorphization occurs in YSZ following the 400 keV Xe irradiation to $3x10^{16}$ Xe/cm^2 even at -170 °C [18]. These observations suggest that point defects produced by ion irradiation are highly mobile in YSZ at cryogenic temperatures. The behavior observed in this study is in strong contrast to that of $MgAl_2O_4$ [8] and α-Al_2O_3 [19], which showed increased lattice disorder with decreasing irradiation temperature due to the reduced mobility of point defects. Therefore, it is expected that an amorphous state would not be readily produced by radiation damage in the materials that do not exhibit enhanced radiation damage with decreasing temperature.

A defect-denuded zone of 60 nm thickness is clearly present in the Xe-irradiated YSZ, in particular up to a dose of $5x10^{15}$ Xe/cm^2 in Figs. 2 and 3. After the $3x10^{16}$ Xe/cm^2 irradiation, the higher minimum yield (~40%) in this zone (Fig. 5) is mostly due to the presence of a high concentration of small Xe precipitates. As determined, the 4 at.% Xe precipitates are distributed uniformly over the depth of 20-110 nm. The XTEM results in Fig. 6(a) show no sign of other larger structural defects within this zone besides the small Xe precipitates. This supports that the precipitates and the resulting strain field may be the major cause for dechanneling in the defect-denuded zone. The denuded zone in YSZ irradiated at -90 °C is similar to that found in $MgAl_2O_4$ spinel following ion irradiation at room temperature [7] or 400 °C [20]. Zinkle has attributed the defect-denuded zone to the effective annihilation of point defects at the surface [7] and to ionization-enhanced diffusion [2].

5. Conclusions

We have studied *in situ* the kinetics of radiation damage accumulation in YSZ under 400 keV Xe ion irradiation at temperatures of 30 and -90 °C. The radiation damage behavior was found to be identical at these two temperatures and no amorphization was observed up to $3x10^{16}$ Xe/cm^2 equal to 110 dpa for peak damage. The irradiated YSZ consisted of a defect-denuded top layer of 60 nm thickness, followed by a highly disordered layer. The lattice disorder reached a saturation level in the bottom layer while its thickness increased towards a great depth (160 nm), deeper than the irradiated depth (<110 nm). XTEM and RBS measurements are interpreted as indicating the presence of small Xe precipitates with an average diameter of 3 nm, uniformly distributed over the 20-110 nm depth. The study demonstrated that radiation-induced point defects are highly mobile, and grow into stable defects in the depth beyond the irradiated region.

Acknowledgments

We are grateful to Caleb Evans, Mark Hollander, and Joseph Tesmer for technical assistance with Xe ion irradiations. All ion beam work was performed at the Los Alamos Ion Beam Materials Laboratory. This research was sponsored by the U.S. Department of Energy, Office of Basic Energy Sciences, Division of Materials Sciences.

References

[1] For a review, see L.W. Hobbs, F.W. Clinard, Jr., S.J. Zinkle, and R.C. Ewing, J. Nucl. Mater. 216 (1994) 291.

[2] For a review, see S.J. Zinkle, Nucl. Instrum. Meth. B 91 (1994) 234.

[3] F.W. Clinard, Jr., G.F. Hurley, and L.W. Hobbs, J. Nucl. Mater. 108-109 (1982) 655.

[4] F.A. Garner, G.W. Hollenberg, F.D. Hobbs, J.L Ryan, Z. Li, C.A. Black, and R.C. Bradt, J. Nucl. Mater. 212-215 (1994) 1087.

[5] K.E. Sickafus, A.C. Larson, N. Yu, M. Nastasi, G.W. Hollenberg, F.A. Garner, and R.C. Bradt, J. Nucl. Mater. 219 (1995) 128.

[6] C. Kinoshita, K. Fukumoto, K. Fukuda, F.A. Garner, and G.W. Hollenberg, J. Nucl. Mater. 219 (1995) 143.

[7] S.J. Zinkle, J. Am. Ceram. Soc. 72 (1989) 1343.

[8] N. Yu, K.E. Sickafus, and M. Nastasi, Philos. Mag. Lett. 70 (1994) 235; N. Yu, M. Nastasi, M.G. Hollander, C.R. Evans, C.J. Maggiore, K.E. Sickafus, and J.R. Tesmer, Mater. Res. Soc. Symp. Proc. 316 (1994) 69.

[9] N. Bordes, L.M. Wang, R.C. Ewing, and K.E. Sickafus, J. Mater. Res. 10 (1995) 981.

[10] J.N. Mitchell, N. Yu, K.E. Sickafus, M. Nastasi, T.N. Taylor, K.J. McClellan, and G.L. Nord, Res. Soc. Symp. Proc. 396, (1996), in press.

[11] N. Yu, M. Nastasi, T.E. Levine, J.R. Tesmer, M.G. Hollander, C.R. Evans, and C.J. Maggiore, Nucl. Instru. Meth. B 99 (1995) 566.

[12] N. Yu, T.E. Levine, K.E. Sickafus, M. Nastasi, J.N. Mitchell, C.J. Maggiore, C.R. Evans, M.G. Hollander, J.R. Tesmer, W.J. Weber, and J.W. Mayer, Nucl. Instru. Meth. B (1995), in press.

[13] E.L. Fleischer, M.G. Norton, M.A. Zaleski, W. Hertl, C.B. Carter, and J.W. Mayer, J. Mater. Res. 6 (1991) 1905.

[14] E.L. Fleischer, W. Hertl, T.L. Alford, P. Børgesen, and J.W. Mayer, J. Mater. Res. 5 (1990) 385.

[15] J.F. Ziegler, J.P. Biersack, and U. Littmark, *The Stopping and Range of Ions in Solids*, (Pergamon, New York, 1985).

[16] Using the RUMP code, L.R. Doolittle, Nucl. Instru. Meth. B 9 (1985) 344.

[17] M.G. Norton, E.L. Fleischer, W. Hertl, C.B. Carter, J.W. Mayer, and E. Johnson, Phys. Rev. B 43 (1991) 9291.

[18] N. Bordes, R.C. Ewing, K.E. Sickafus, and M. Nastasi, to be published, (1996).

[19] C.J. McHargue, G.C. Farlow, C.W. White, J.M. Williams, B.R. Appleton, and H. Naramoto, Mater. Sci. Engin. 69 (1985) 123.

[20] N. Yu, K.E. Sickafus, and M. Nastasi, Mater. Res. Soc. Symp. Proc. 373 (1995) 401.

Figure captions:

Figure 1 Schematic drawings of *in situ* characterization of ion-irradiation induced phenomena using transmission electron microscopy and ion-beam analysis.

Figure 2 *In situ* RBS/C spectra obtained from an YSZ crystal using a 2 MeV He ion-beam incident along the (011) axis following sequential 400 keV Xe irradiations at 30 °C, along with a random spectrum from the YSZ crystal irradiated to the highest dose.

Figure 3 *In situ* RBS/C spectra obtained from an YSZ crystal using a 2 MeV He ion-beam incident along the (011) axis following sequential 400 keV Xe irradiations at -90 °C, along with a random spectrum from the YSZ crystal irradiated to the highest dose.

Figure 4 The minimum yield of Zr from the highly disordered zone in YSZ versus Xe irradiation dose at the irradiation temperatures of 30 and -90 °C.

Figure 5 *Ex situ* RBS/C spectra obtained from the YSZ crystals using a 2 MeV He ion-beam incident along the (001) axis before and after the Xe irradiations of 400 keV and $3x10^{16}$ Xe/cm^2 at 30 and -90 °C, respectively, along with a random spectrum from the unirradiated sample.

Figure 6 (a) Dark-field XTEM image showing a Xe-rich layer (labeled "1") and a highly defected layer ("2"), followed by the unirradiated YSZ substrate ("3"), with g=[$\bar{1}\bar{1}1$], along with (b), (c), and (d) microdiffraction patterns taken from the zones "1, 2, and 3", respectively.

Figure 7 Schematic drawing showing evolution of accumulation of implanted Xe ions and structural defects in the Xe-irradiated YSZ from a low dose (top) to a high dose (bottom).

ANL *in situ* Experiment

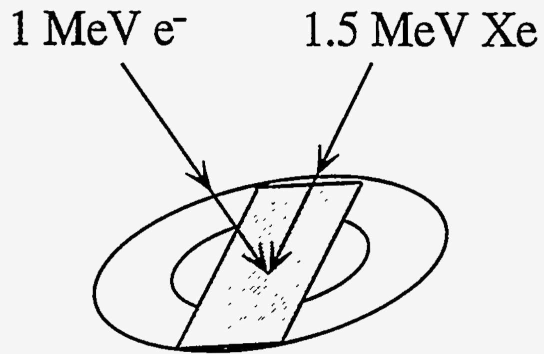

LANL *in situ* Experiment

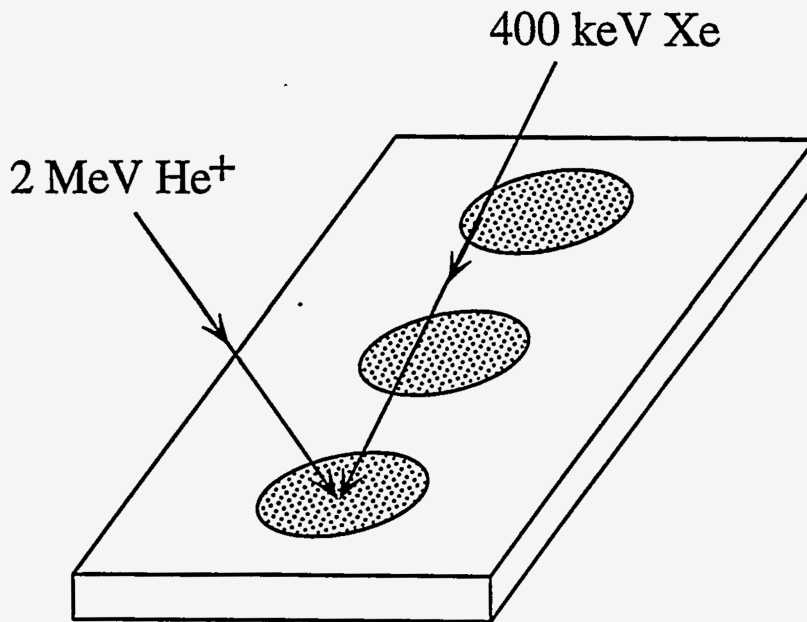

Fig. 1

N. Yu et

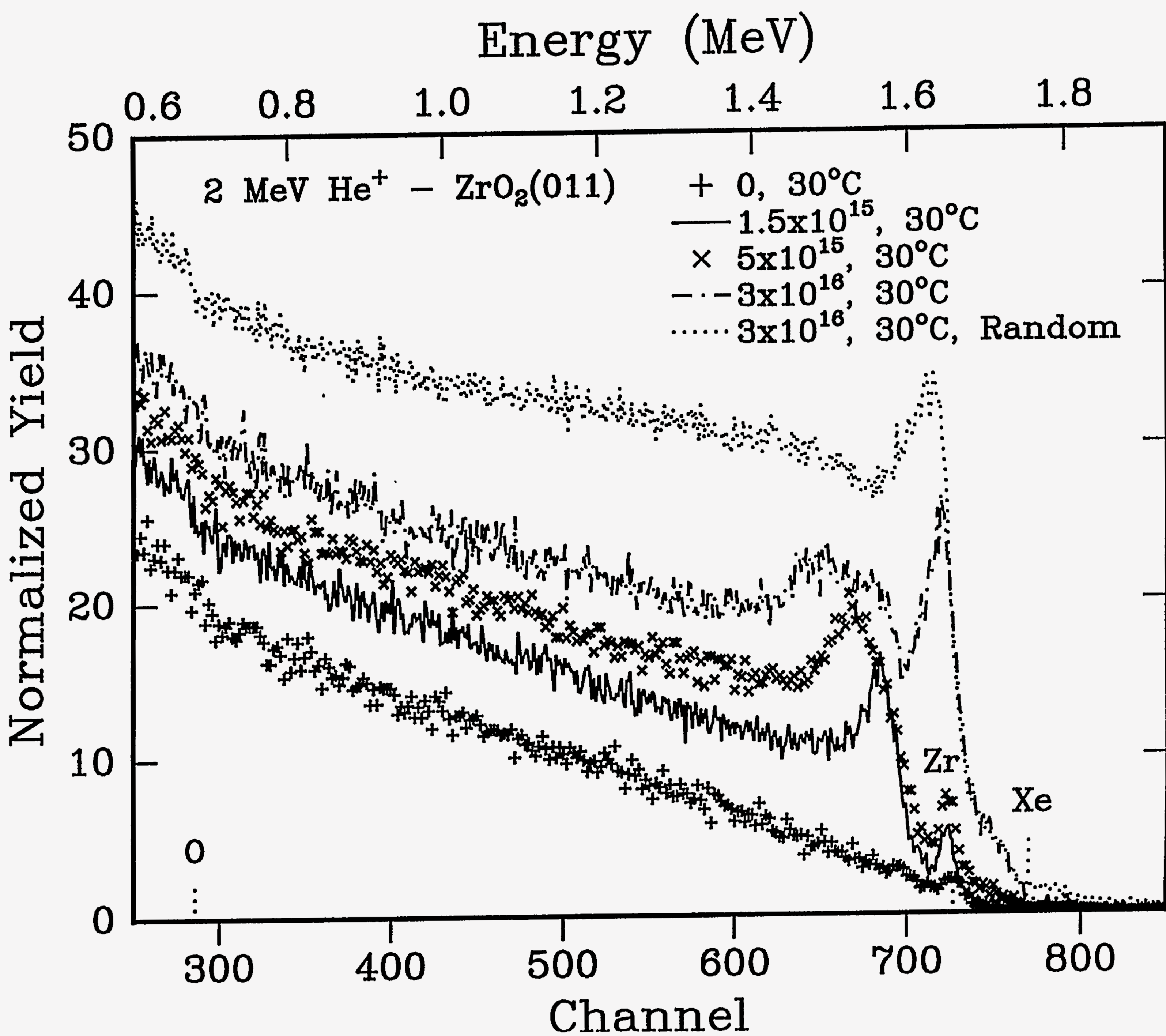

Energy (MeV)
0.6
0.8
1.0
1.2
1.4
1.6
1.8
Normalized Yield
50
40
30
20
10
0
2 MeV He+ – ZrO2(011)
+ 0, 30°C
1.5x10^15, 30°C
× 5x10^15, 30°C
3x10^16, 30°C
3x10^16, 30°C, Random
O
Zr
Xe
300
400
500
600
700
800
Channel

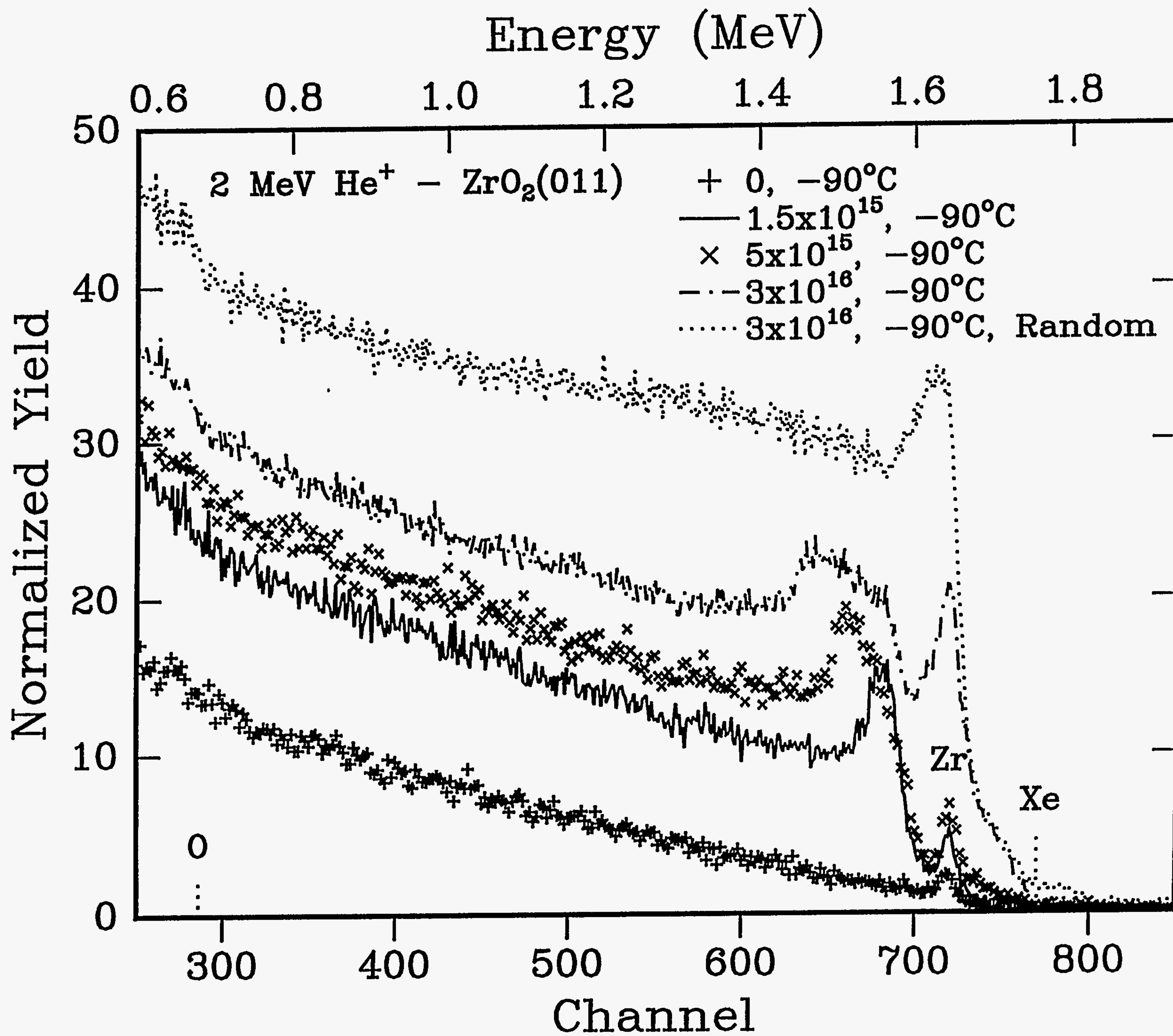

Fig. 3

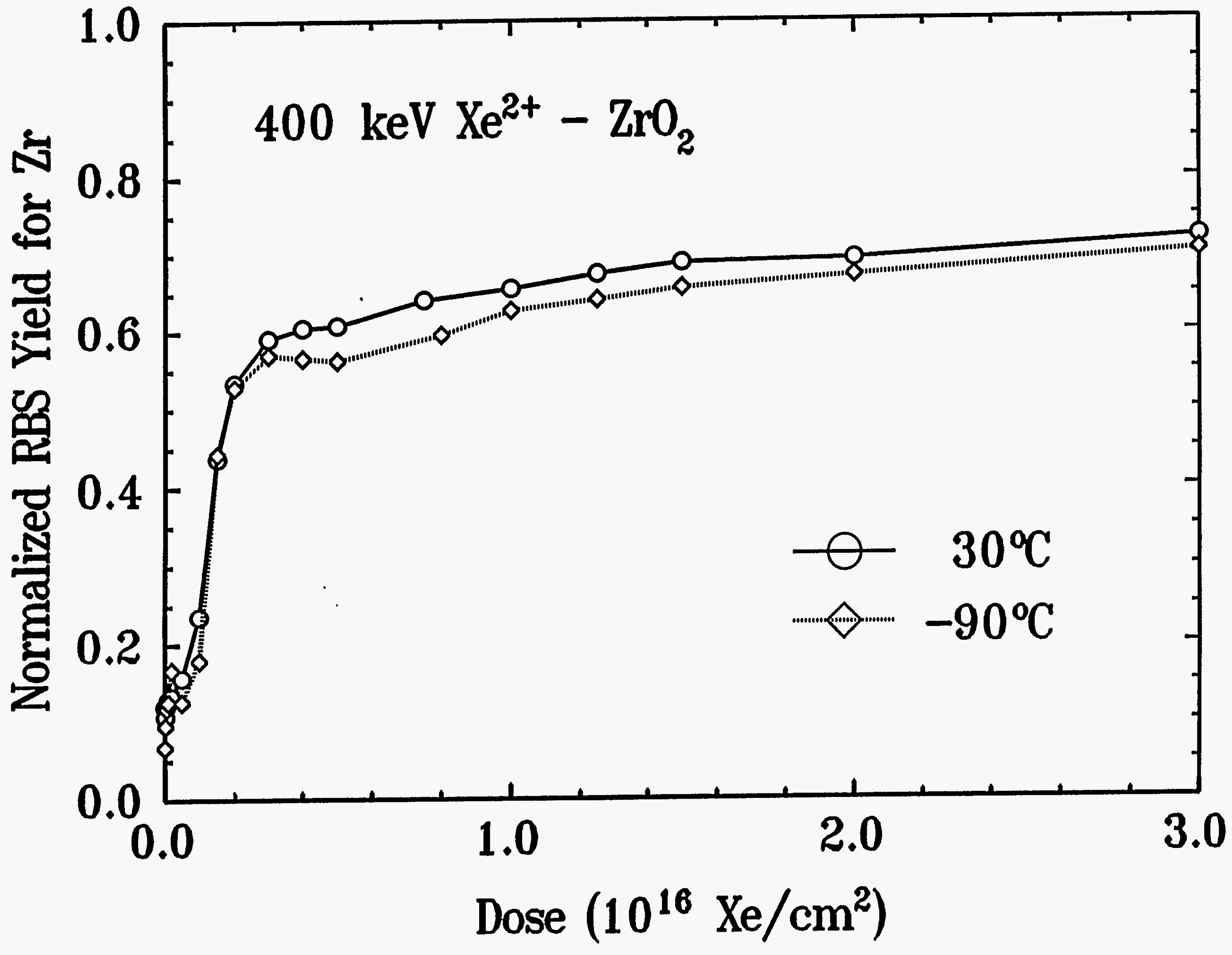

Fig 1L

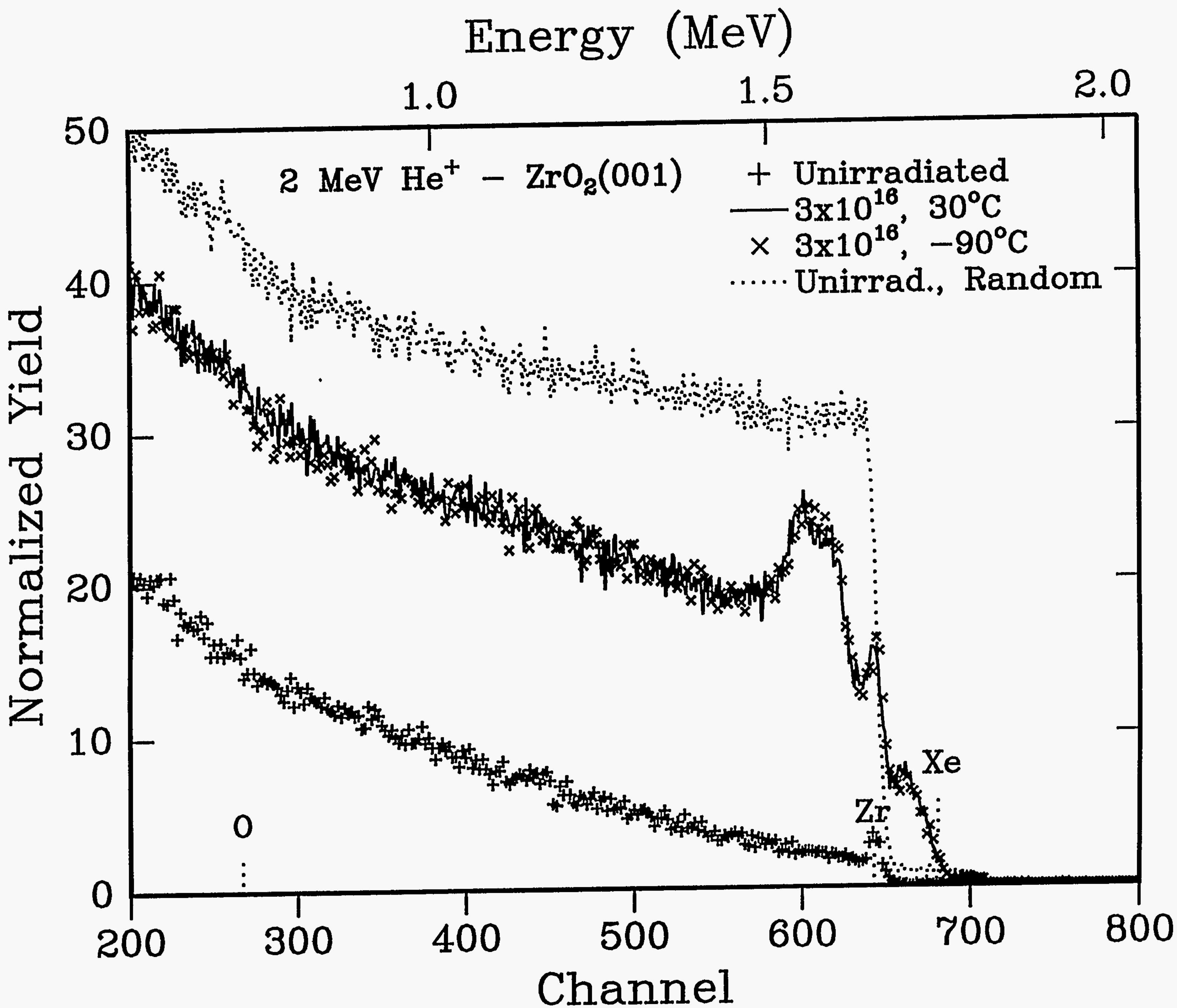

Fig 5

(a) Surface

1

2

3

100 nm

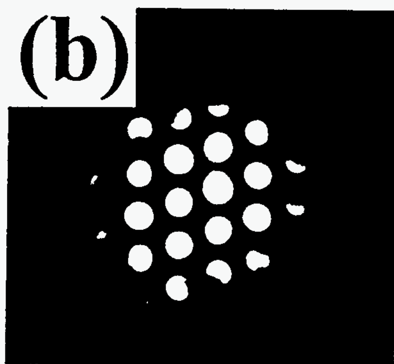

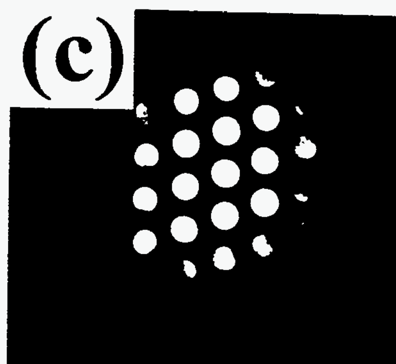

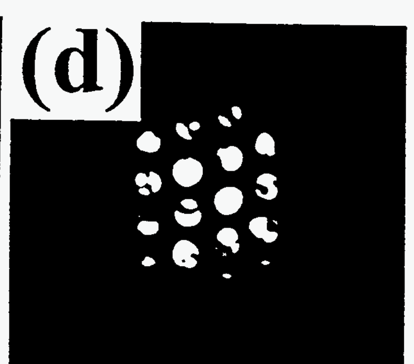

Yu et al. Fig 6

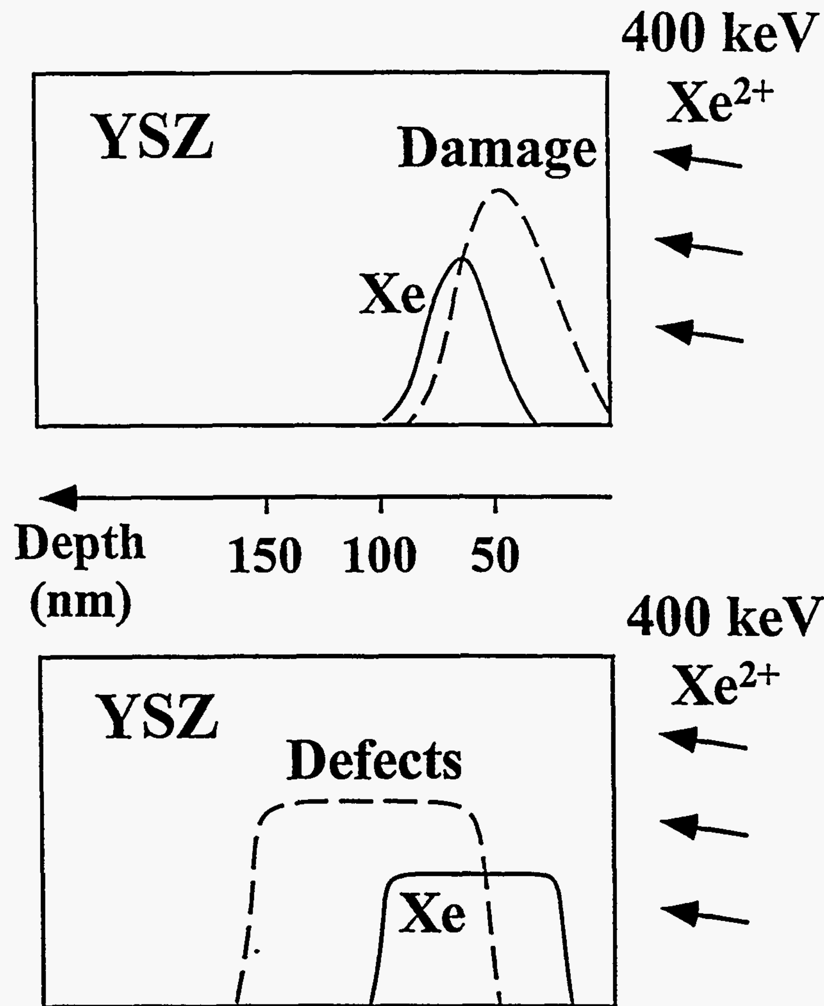

DISCLAIMER

This report was prepared as an account of work sponsored by an agency of the United States Government. Neither the United States Government nor any agency thereof, nor any of their employees, makes any warranty, express or implied, or assumes any legal liability or responsibility for the accuracy, completeness, or usefulness of any information, apparatus, product, or process disclosed, or represents that its use would not infringe privately owned rights. Reference herein to any specific commercial product, process, or service by trade name, trademark, manufacturer, or otherwise does not necessarily constitute or imply its endorsement, recommendation, or favoring by the United States Government or any agency thereof. The views and opinions of authors expressed herein do not necessarily state or reflect those of the United States Government or any agency thereof.

Yu et al. Fig. 7